OPTICA

Strong interactions between integrated microresonators and alkali atomic vapors: towards single-atom, single-photon operation

Roy Zektzer,[1,2,5] Xiyuan Lu,[1,2] Khoi Tuan Hoang,[1] Rahul Shrestha,[1] Sharoon Austin,[1,3] Feng Zhou,[1,2] Ashish Chanana,[2] Glenn Holland,[2] Daron Westly,[2] Paul Lett,[1,4] Alexey V. Gorshkov,[1,3,4] and Kartik Srinivasan[1,2,*]

[1]Joint Quantum Institute, NIST/University of Maryland, College Park, Maryland 20742, USA
[2]Microsystems and Nanotechnology Division, National Institute of Standards and Technology, Gaithersburg, Maryland 20899, USA
[3]Joint Center for Quantum Information and Computer Science, NIST/University of Maryland, College Park, Maryland 20742, USA
[4]Quantum Measurement Division, National Institute of Standards and Technology, Gaithersburg, Maryland 20899, USA
[5]roy.zektzer@umd.edu
*kartik.srinivasan@nist.gov

Received 4 April 2024; revised 22 August 2024; accepted 3 September 2024; published 24 September 2024

Cavity quantum electrodynamics (cQED), the interaction of a two-level system with a high quality factor (Q) cavity, is a foundational building block in different architectures for quantum computation, communication, and metrology. The strong interaction between the atom and the cavity enables single-photon operation, which is required for quantum gates and sources. Cold atoms, quantum dots, and color centers in crystals are among the systems that have shown single-photon operations, but they require significant physical infrastructure. Atomic vapors, on the other hand, require limited experimental infrastructure and are hence much easier to deploy outside a laboratory, but they consist of an ensemble of moving atoms that results in short interaction times involving multiple atoms, which can hamper quantum operations. A solution to this issue can be found in nanophotonic cavities, where the optical mode is confined to a small volume and light-matter interaction is enhanced, so that fast single-atom, single-photon operations are enabled. In this work, we study the interaction of an atomically clad microring resonator (ACMRR) with different-sized ensembles of Rb atoms. We demonstrate strong coupling between an ensemble of ≈ 50 atoms interacting with a high quality factor ($Q = 4.3 \times 10^5$) ACMRR, yielding a many-atom cooperativity $C = (5.5 \pm 0.3)$. We continue to observe signatures of atom-photon interaction for a few (<3) atoms, for which we observe saturation at the level of a few intracavity photons. Further development of our platform, which includes integrated thermo-optic heaters to enable cavity tuning and stabilization, should enable the observation of interactions between single photons and single atoms.

https://doi.org/10.1364/OPTICA.525689

1. INTRODUCTION

Single-photon gates, sources, detectors, and memories [1–5] are among the basic building blocks for optical quantum computers, simulators, and communications systems [6,7]. In most architectures, a key aspect of these devices is the ability to generate a strong interaction between single photons and a medium. Chip-scale integration of such devices has the advantage of scalability and miniaturization and the opportunity to decrease the interaction volume and improve light-matter interaction, particularly in the context of cavity quantum electrodynamics (cQED) [8,9]. Indeed, by integrating single solid-state quantum emitters with nanophotonic cavities, single-photon sources and devices exhibiting nonlinearity at the single-photon level have been demonstrated [3,10–13]. Alternately, single cold atoms coupled to a nanophotonic cavity have been used for gate formation [14,15] and are being advanced to enable study of new regimes of strong coherent interactions [16], while ensembles of rare earth ions embedded in nanophotonic cavities have been used as a quantum memory [17,18]. Heterogeneous or hybrid integration [19] further allows the incorporation of such devices with the established silicon nitride (Si_3N_4, hereafter SiN) photonic integrated circuit platform, as was done for on-demand single-photon sources via wafer bonding and subsequent device processing [20] or by placing an already fabricated superconducting single-photon detector directly on a waveguide [21]. While there are thus many systems through which foundational quantum resources can be constructed, they all typically require significant physical infrastructure for operation. This includes cryostats for solid-state systems and magneto-optical trapping in ultra-high vacuum for cold atom systems.

Recently, a comparatively simple quantum technology has been demonstrated, the atomic-cladded waveguide (ACWG) [22], following foundational cQED work with thermal atomic beams [23,24] and subsequent works exploring the interaction

of atomic vapors with hollow core fibers [25,26], hollow core waveguides [27], and tapered fibers [28–30]. The technology is based on bonding an alkali vapor cell onto a photonic chip, resulting in a standalone system that can then operate at room (or slightly elevated) temperature and does not require any vacuum, cryogenic, or trapping infrastructure, and is part of the broader effort to realize chip-based atomic devices for many applications, including in clocks, sensing, and metrology [31]. Such devices have presented chirality [32,33], strong nonlinearity in the telecom regime [34,35], and Autler-Townes splitting [36]. A key parameter to evaluate light-matter interaction in cQED is the collective cooperativity $C = g^2/2\kappa\gamma$, where g is the coupling rate between the ensemble of atoms and the cavity and κ and γ are the cavity field decay and atomic dephasing rate, respectively [9]. Taking N as the number of atoms interacting with the field, C can be related to the single-atom cooperativity C_0 by $C = NC_0$ in the limit that all N atoms interact with the field uniformly; in this case $g = \sqrt{N}g_0$, where g_0 is the coupling rate between a single atom and the cavity field. The short-time interaction of fast-moving atoms (300 m/s) with a nanoscale optical mode limits the atomic state's coherence [29], resulting in $\gamma/2\pi = 200$ MHz [22,37] (instead of the natural linewidth of 6 MHz). The excess broadening can affect metrological applications [38], and may also impact single-photon operations, at a minimum, by limiting the number of operations that can occur before the atom leaves the cavity. The transit time limitation can be avoided for metrological applications by diffracting light from the waveguide into a large, free-space beam that is emitted from the photonic chip [39,40], but this will reduce light-matter interaction significantly. On the other hand, it has been suggested that the large coupling strengths in nanophotonic cavities can overcome the excess broadening in warm atoms resulting from transit time, so that even single-atom-single-photon strong coupling in cQED may be observable [37]. Working towards that regime, collective cooperativity of $C = 42$ has recently been demonstrated with an 80 μm radius microdisk resonator coupled to a dense ensemble of Rb atoms [41], following earlier work in which Rb interactions with low quality factor cavities were studied [42,43].

Here, we develop an integrated photonics platform [Fig. 1(a)] that combines air-clad microring resonators and Rb vapor, with integrated buried heaters enabling a resonator mode to be frequency locked for long-term stable operation. We demonstrate strong coupling between an ensemble of ≈ 50 atoms interacting with a high Q (4.3×10^5, $\kappa/2\pi = 445$ MHz) and small volume (20 μm radius) cavity mode, with a many-atom coupling strength $g/2\pi = 1$ GHz and many-atom cooperativity $C = (5.5 \pm 0.3)$ achieved. We also study these vapor cQED devices at lower atomic densities, and while vacuum Rabi splitting is no longer seen at the lowest density, we continue to observe saturation effects in the cavity transmission when <3 atoms are in the cavity on average, with saturation occurring for a few photons in the cavity on average. With improvements to the cavity parameters–in particular a reduction in size to increase g_0, for example, using photonic crystal ring resonator devices [44,45]–strong coupling between single vapor-phase atoms and single photons should be achievable.

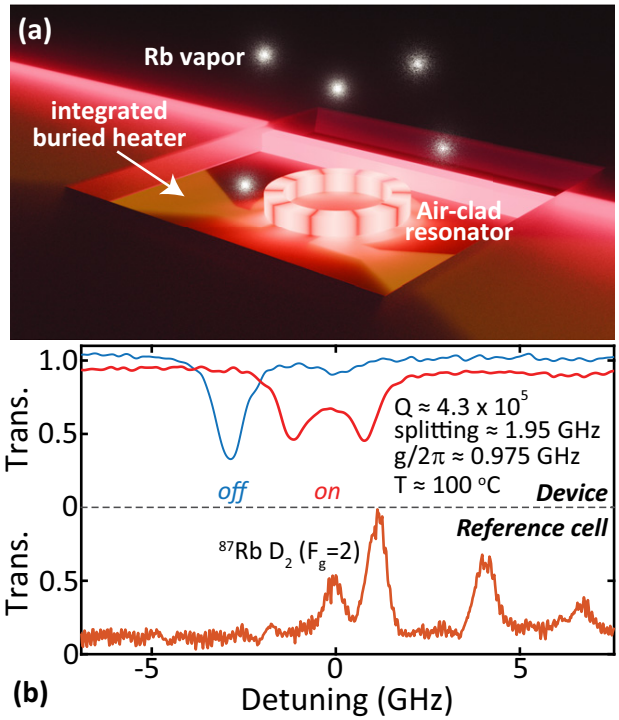

Fig. 1. System and initial results. (a) Illustration of the platform developed in this work, where atoms from a Rb vapor interact with the evanescent field of an air-clad resonator. We utilize integrated heaters that are buried underneath the lower waveguide cladding for resonator tuning and stabilization, enabling measurements in the low atom, low photon regime. (b) Initial results in a device without buried heaters. (Top) Representative cavity transmission measurement off-resonance (blue) and on-resonance (red) with the ^{87}Rb D_2 transition ($5S_{1/2}(F = 2) \rightarrow 5P_{3/2}(F = 1, 2, 3)$) of an ensemble of ≈ 50 Rb atoms (temperature of 100°C). These measurements are taken from a device without integrated buried heaters; measurements in subsequent figures use stabilization. (Bottom) Simultaneously recorded absorption spectrum of a Rb reference cell containing both ^{87}Rb and ^{85}Rb (the cavity device only contains ^{87}Rb).

2. INITIAL RESULTS AND IMPROVED DEVICE PLATFORM

Our device platform concept is illustrated in Fig. 1(a), where moving atoms interact with the microring resonator (MRR) mode and integrated heaters enable control of the cavity mode frequency. Before implementing this full platform, we first consider devices without the heaters and focus on understanding the potential degradation of cavity Q in the presence of Rb vapor. We fabricate SiN MRR devices with a radius of 20 μm, thickness of 250 nm, and ring width of 1 μm according to a standard SiN process flow, bond a borosilicate glass cell to the chips using vacuum epoxy, and send them to a commercial vendor who evacuates and fills them with pure ^{87}Rb (see Supplement 1). As the chip facets are outside the cell region, coupling into and out of the chips can be done using standard approaches with lensed optical fibers. By keeping the cell pinch-off point sufficiently far from the photonic chip, we can limit the potential contamination of the integrated photonics devices during the cell filling process.

We install the devices in a measurement setup that has dedicated heater mounts for both the chip and the cell (see Supplement 1). Setting each at a temperature of 100°C, we first perform swept-wavelength spectroscopy of cavity modes that are off-resonance

from the Rb transitions [top panel of Fig. 1(b)], along with simultaneous characterization of a reference Rb cell containing both ^{87}Rb and ^{85}Rb [bottom panel of Fig. 1(b)]. We measure optical modes with Q as high as $(4.3 \pm 0.1) \times 10^5$ when detuned from the Rb transitions, where the uncertainty is taken as the 95% confidence interval in a nonlinear least squares fit of the data to a standard resonator-waveguide transmission model. By adjusting the chip temperature, we tune the mode into the ^{87}Rb $F = 2$ transition and observe its pronounced splitting, by (1.95 ± 0.05) GHz, where the uncertainty is a one standard deviation value associated with determining the positions of the two minima in the Rabi-split spectrum. We note that the ^{87}Rb $F = 1$ transition (the rightmost peak in the reference cell spectrum) is too far-detuned from the cavity mode to interact with it, while unlike the reference cell, the device does not contain ^{85}Rb (the two central peaks in the reference cell spectrum). Thus, a simple single splitting of the cavity mode is observed.

The splitting in the on-resonance spectrum is twice the many-atom coupling rate $g/2\pi = (0.98 \pm 0.02)$ GHz. The cavity field decay rate (κ) is given by the off-resonance half linewidth (445 MHz). Assuming a decay rate $\gamma/2\pi = 200$ MHz (controlled by the transit time), we obtain a collective cooperativity $C = g^2/2\kappa\gamma = (5.5 \pm 0.3)$. From the cell temperature of 100°C, we expect an equilibrium Rb density of 4.7×10^{18} m^{-3} [46], which for a simulated cavity volume of 11.2 μm^3 gives an estimate of $N = 53$ atoms interacting with the cavity. The average single-atom cooperativity $C_0 = C/N = 0.1$, which assumes that every atom interacts with the field equally. In Section 2 of Supplement 1, we present a comparison of the experimental data in Fig. 1(b) with many-atom cQED simulations that take into account the spatial variation of the field and that average over many distributions of the atomic velocities and spatial positions. We find that the results match well (Fig. S3) and are consistent with an atom in the strongest part of the cavity field experiencing $g_0/2\pi = 330$ MHz, corresponding to $C_0 = 0.61$. This value of g_0 is in turn consistent with expectation based on finite-element method simulation of the optical cavity mode profile.

These initial measurements verify that high Q can be preserved in the presence of Rb and that vacuum Rabi splitting due to the contribution of a few dozen atoms can be observed. To probe this system more carefully, and in particular in the limit of a small number of atoms and with a single-photon-level intracavity field, requires long averaging times, which demands fine control over the cavity detuning and elimination of any thermal drifts, as $\delta T = 20$ mK shifts in temperature result in $\delta f = 100$ MHz shifts in the cavity mode frequency. This can be seen given the relationship $(\delta f)^2 = [f/n_{\text{eff}}(dn_{\text{eff}}/dT)]^2(\delta T)^2$, where f is the cavity mode frequency, n_{eff} is the cavity mode effective index, and dn_{eff}/dT is the effective thermorefractive coefficient for the cavity mode, which is approximately equal to the material thermorefractive coefficient $dn/dT = 2.4 \times 10^{-5}$ K^{-1}. Next, we will explain how our new platform and experimental setup achieve this needed stability. The platform [Figs. 2(a)–2(d)] consists of a 250 nm thick Si_3N_4 waveguide layer, underlying metallic heater, and lower SiO_2 cladding layers, and an upper cladding that is air near the resonators (for Rb interaction) and SiO_2 everywhere else (for cell bonding and facet coupling), with more details provided in Supplement 1. Figure 2(a) shows a photograph of a completed device, highlighting that both the waveguide facets and electrical contact pads are outside the cell region and therefore accessible.

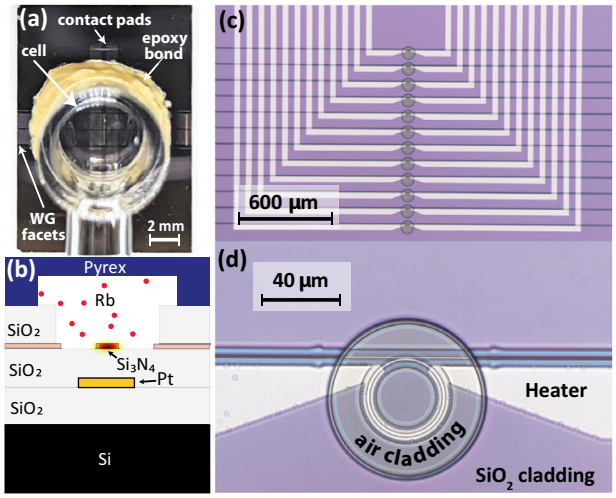

Fig. 2. Experimental platform: an atomically clad microring resonator (ACMRR) chip integrated buried heaters. (a) Photograph of a completed device, with important features indicated. (b) Cross-sectional schematic of the vapor-cavity interaction region. (c), (d) Optical microscope images of the fabricated photonic chip, with the heater traces, SiO_2 cladding, and air cladding regions indicated.

Figure 2(b) shows a schematic cross-section indicating the material layer stack, while Figs. 2(c) and 2(d) show optical microscope images of a fabricated photonic chip, indicating the air-clad resonator, SiO_2-clad waveguide, and heater regions.

3. SETUP STABILITY AND ANTI-CROSSING SPECTROSCOPY

Our measurement setup for interrogating the ACMRRs with integrated buried heaters is depicted in Fig. 3(a). We place fabricated samples in a setup in which both the chip and glass cell have independent proportional-integral-derivative (PID) temperature control (see Supplement 1) along with the device-level fine temperature control provided by the integrated heaters. We couple to the chips using 780 nm band lensed optical fibers and achieve a per facet coupling loss of (8.5 ± 0.5) dB, where the uncertainty is a one standard deviation value based on measuring the insertion losses of many devices, and this quantity also includes any loss in the transition between the oxide-clad and air-clad regions on the chip. We proceed to tune a high Q resonance to the ^{87}Rb $F = 2$ transition in a coarse fashion by setting the chip holder temperature to 117°C. To fine-tune the position of the resonance and ensure stability for long-term measurements, we stabilize the MRR temperature by locking its mode around 770 nm to a laser using the buried heaters [47], with the laser wavelength stabilized by feedback from a wavemeter. The device interrogation is done by a second laser at 780 nm. Cross-talk between the locking system and measurement system is avoided by placing bandpass filters before and after the device. Using the error signal from the lock-in amplifier we estimate the MRR mode frequency stability and extract its Allan deviation when locked and unlocked [Fig. 3(b)]. The MRR long-term stability drifts by more than 100 MHz when unlocked, which is sufficiently close to the mode linewidth to be a problem for long-term measurements. However, when locked, the mode stability is at the <1 MHz level, making long-term measurements possible. We note that this Allan deviation represents our ability to lock the mode to the laser, which is locked to the wavemeter. For

the type of wavemeter we utilize, other studies have shown that stability at the level of a few MHz is possible [48]. In addition, the locking parameters have been optimized for stability at the time scales of relevance to the measurements we will perform in this work, but different locking parameters may be chosen to improve performance at shorter time scales if desired. The shortest time scale over which feedback will be effective is determined by the response bandwidth of the heaters, which in the current implementation is relatively low (near 1 kHz). Higher bandwidths near 30 kHz have been demonstrated by lowering the resistance of the electrical traces [49].

We seek to probe the devices in the regime of small numbers of atoms and photons in the cavity. The number of photons in the cavity is controlled by the input power into the waveguide on the chip, and is on the order of 1 nW for an average intracavity photon number near one. Optical power is calibrated by determining the insertion losses of the components in the optical setup and the aforementioned facet coupling loss, with the power meter on the input side of the chip in the setup in Fig. 3(a) enabling relative changes in power to be easily determined in real-time. The one standard deviation uncertainty in on-chip power, dominated by the uncertainty in coupling loss, is 15%. The number of atoms is determined by the vapor temperature, which is controlled by a heater embedded within a copper shroud that surrounds the cell (see Supplement 1). We estimate the vapor temperature using a free-space system [Fig. 3(a)] that interrogates the cell through its top window. Measuring the transmission of a signal reflected from the chip and fitting it to a standard model [50] [Fig. 3(c)] provides an estimate of the vapor temperature that is generally consistent with the temperature reading on the copper shroud.

Next, we tune the cell temperature to 120°C and measure the low power device transmission by scanning an attenuated 780 nm laser across the cavity resonance. We tune the chip temperature by 1°C using the buried heaters to shift the MRR mode across the Rb D2 transitions. We present a sample of the data in Fig. 3(d) and the full set of spectra in Fig. 3(e). Clear anti-crossing and Rabi splitting are observed as the cavity crosses both ^{87}Rb D2 ground state transitions.

4. MEASUREMENTS AT REDUCED ATOM NUMBER DOWN TO THE FEW-ATOM REGIME

We next study the on-resonance saturation behavior of the system, with the cavity spectral position fixed using a wavelength modulation locking setup with feedback to the buried heaters, as indicated in Fig. 3(a). We investigate the atom-cavity interaction at various cell temperatures and input powers (Fig. 4), focusing on changes in the transmission spectrum, which we normalize to the mean off-resonance value for a given set of conditions. We observe reduced splitting as we saturate the atoms (i.e., at higher optical powers) and decrease the atomic density, moving from a regime of a few dozen atoms (e.g., at 100°C) to a regime of a few atoms (e.g., at 60°C). A clear splitting in the low power spectrum is observed down to ≈ 50 atoms in the cavity, yet is slightly less prominent compared to the results shown in Fig. 1 as the device with the buried heaters has $Q = (2.29 \pm 0.03) \times 10^5$ compared to $Q = (4.3 \pm 0.1) \times 10^5$ for the device without heaters. The reduction in Q for the integrated heater devices requires further investigation. While in previous work $Q = 7.5 \times 10^5$ was demonstrated with heaters incorporated [49], those devices operated in a regime of stronger

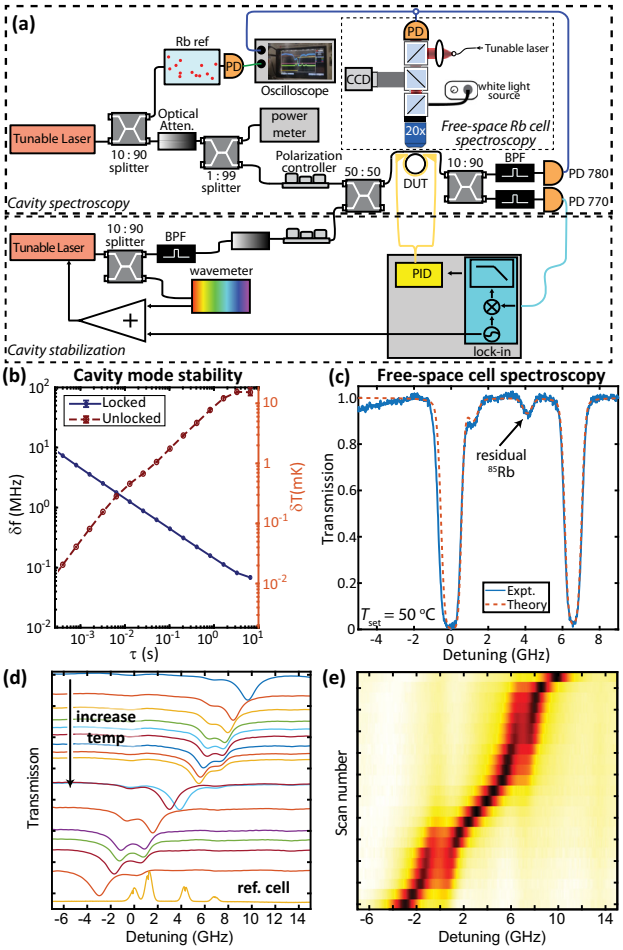

Fig. 3. Measurement setup and anti-crossing spectroscopy. (a) Schematic illustration of the measurement setup. The top dashed box indicates the cavity spectroscopy portion, where a tunable laser is split to simultaneously interrogate a reference Rb cell and the cavity-vapor device at wavelengths near the Rb D2 transition. The same laser can be sent to interrogate the device in free-space (inner dashed box), to provide a consistency check on the vapor density estimated from the set cell temperature. The bottom dashed box indicates the cavity stabilization portion, based on simultaneous probing of a second cavity resonance (detuned from Rb) and feedback to chip-integrated heaters. PD: photodetector; CCD: charge-coupled device; DUT: device under test; BPF: bandpass filter; PID: proportional-integral-derivative. (b) Allan deviation of the cavity mode frequency shift (left y-axis) and temperature (right y-axis) over time when locked (blue) and unlocked (red). (c) Representative free-space spectroscopy of the device cell region at a temperature of 50°C, along with the expected result from a theoretical model (dashed line). (d), (e) Device cavity transmission for different detunings of the MRR from the ^{87}Rb D2 transitions, showing vacuum Rabi splitting and anti-crossing. The cavity temperature is changed by 1°C from the top scan to the bottom scan using the buried integrated heaters. The bottom spectrum in (d) is taken from the reference cell.

modal confinement and hence reduced sensitivity to the underlying SiO_2 layer, which is of a different type than that used in devices without heaters (see Supplement 1 Section 1 for more fabrication details). In addition, different lithography conditions were used when patterning the microrings for the integrated heater devices.

While splitting is no longer present at the lowest densities, we still find an observable difference between the low power and high power spectrum, and hence a signature of the atom-cavity interaction, at the lower temperatures. This difference

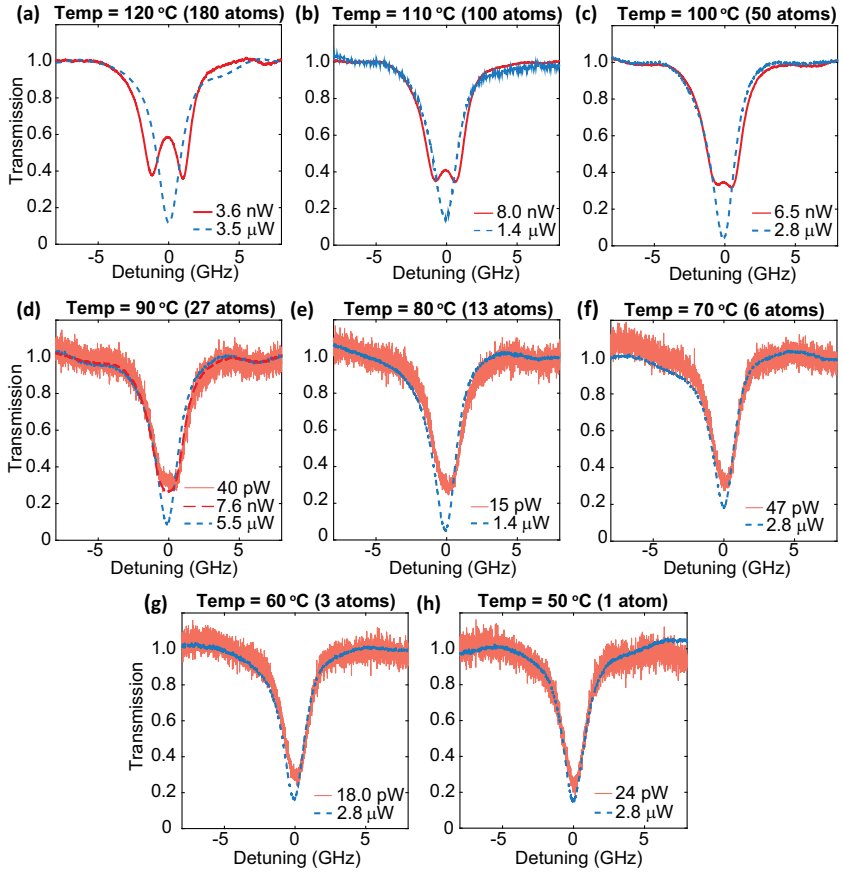

Fig. 4. High power, low power, and few-photon-level cavity transmission as a function of vapor temperature. (a)–(c) High power (dashed blue) and low power (dark red) cavity transmission spectrum when on resonance with the Rb $F = 2$ transition at a vapor temperature of 120°C (a), 110°C (b), and 100°C (c). (d) High power (dashed blue), low power (dashed dark red), and few-photon-level power (light red) at a vapor temperature of 90°C. (e)–(h) High power (dashed blue) and few-photon-level (light red) cavity transmission spectrum when on resonance with the Rb $F = 2$ transition at a vapor temperature of 80°C (e), 70°C (f), 60°C (g), and 50°C (h). In (d) a slight difference is observed between the few-photon-level and low power data, indicating the onset of atomic saturation, while in (e)–(h) we focus on the comparison between the few-photon-level and high power results. The estimated number of atoms within the cavity near-field is listed in each sub-panel. The cavity transmission is normalized to the mean value off-resonance. The optical powers listed are on-chip at the waveguide input, and have a one standard deviation uncertainty of 15%.

is observable even at 50°C, where it is estimated that only one atom interacts with the cavity on average. For example, from the spectra in Fig. 4, we can examine the change in normalized transmission contrast on resonance ($\Delta T_{\mathrm{hp-lp}}$) between the high power and low power cases. At 50°C, we find that $\Delta T_{\mathrm{hp-lp}} = (T_{\mathrm{hp,off}} - T_{\mathrm{hp,on}})/T_{\mathrm{hp,off}} - (T_{\mathrm{lp,off}} - T_{\mathrm{lp,on}})/T_{\mathrm{lp,off}} = (0.15 \pm 0.10)$, where $T_{\mathrm{lp,on}}$ ($T_{\mathrm{hp,on}}$) is the low power (high power) on-resonance transmission value and $T_{\mathrm{lp,off}}$ ($T_{\mathrm{hp,off}}$) is the low power (high power) off-resonance transmission value. The uncertainty is a one standard deviation value that is dominated by the noise in the off-resonance signal at low power (i.e., in $T_{\mathrm{lp,off}}$). This value can be compared to $\Delta T_{\mathrm{hp-lp}}$ in the case where we tune the cavity off of the Rb transition (i.e., so that there is no atom-cavity interaction in either the high power or low power limit). This baseline measurement yields $\Delta T_{\mathrm{hp-lp}} = (0.07 \pm 0.10)$, indicating that when the cavity is aligned with the Rb transition at 50°C, the data does show a signature of atom-cavity interaction.

Given the relatively large uncertainty when comparing just two spectra, a more conclusive comparison can be provided by tracking changes in the transmission spectrum for a range of input powers. In Fig. 5(a), we compare such data at {80, 70, 50}°C, and in Fig. 5(b) we show a case where the cavity is off-resonance from the Rb atoms and no atom-cavity interaction is expected. Here, we plot the splitting as a function of input power in the waveguide, where the splitting is determined by a double oscillator fit to the normalized transmission data and the error bars are 95% confidence intervals for those fits. A clear trend of reduced splitting as power increases is seen at all temperatures in Fig. 5(a), consistent with saturation of the atomic-cavity interaction, while in the off-resonance data of Fig. 5(b) no trend is observable, as expected. However, we note that the fits to the off-resonance data yield a mean non-zero splitting, even though no splitting is expected. This indicates a limitation of this simple empirical fitting approach for the acquired data, particularly in the regime where any splitting is much smaller than the cavity resonance linewidth of 1.7 GHz.

5. FEW-PHOTON-LEVEL SATURATION

We can get a first estimate of the number of photons in the cavity (n_{cav}) needed to saturate the system based on the data from Fig. 5 and the expression $n_{\mathrm{cav}} = \Delta T P_{\mathrm{in}} Q_T / ((1 + \sqrt{1 - \Delta T})\hbar\omega_0^2)$, assuming an undercoupled cavity (as is the case in our system) [51]. Using a measured loaded quality factor (Q_T) of 2.3×10^5, transmission contrast (ΔT) of 0.8, and angular frequency (ω_0) on

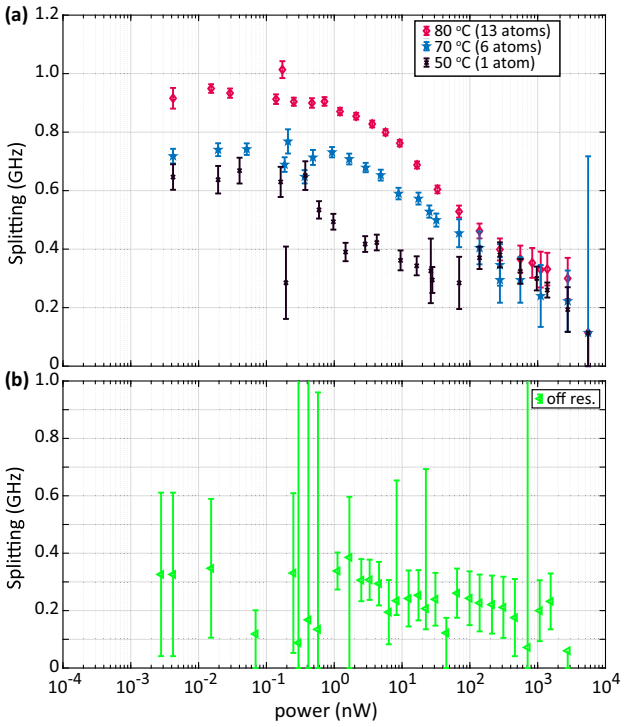

Fig. 5. Saturation of the atom-cavity system in the few-atom regime. (a) Splitting in the cavity transmission spectrum as a function of power for a vapor temperature of {80, 70, 50}°C, corresponding to an average of {13, 6, 1} atoms in the cavity. (b) Splitting data when the cavity is tuned off-resonance from the Rb transition. The splittings are determined by fitting the transmission responses to a double oscillator model, and the error bars are 95% confidence intervals from these fits. As expected, the off-resonance data shows no trend with power. However, the expected splitting value in (b) is zero, indicating the limits to which this approach can be used with the acquired data to reliably infer the presence of atom-cavity interactions. The optical powers are on-chip at the waveguide input and have a one standard deviation uncertainty of 15%.

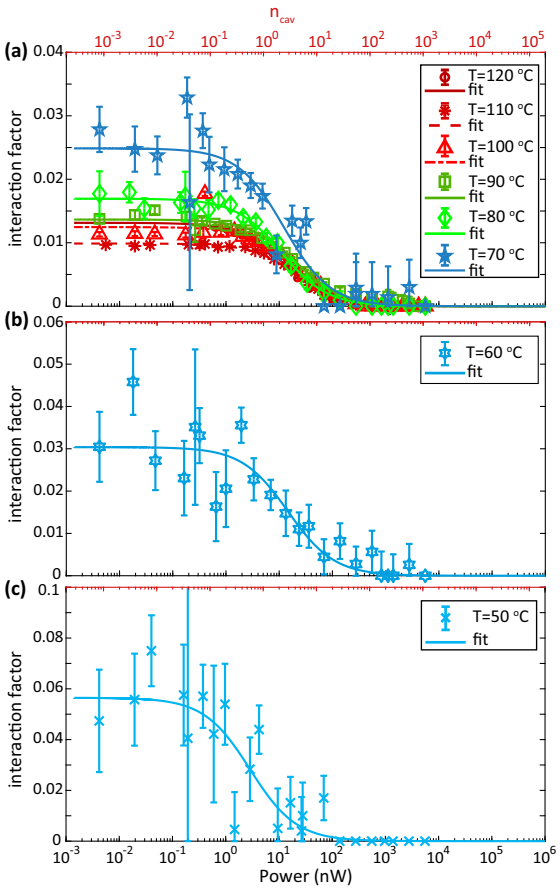

Fig. 6. Interaction factor as a function of vapor temperature. (a) Temperatures between 120°C and 70°C ({180, 100, 50, 27, 13, 6} atoms in the cavity). (b) Temperature of 60°C (three atoms in the cavity). (c) Temperature of 50°C (one atom in the cavity). Symbols are experimental data points and solid curves are fits to the data. The error bars represent 95% confidence intervals and are due to vapor temperature uncertainty and difficulty in separating fit parameters as the Rabi splitting becomes significantly smaller than the cavity linewidth. The optical powers are on-chip at the waveguide input and have a one standard deviation uncertainty of 15%.

the Rb D_2 resonance, we estimate $n_{\mathrm{cav}} \approx 2.1$ for an optical power of 10 nW in the waveguide, which is a power for which significant reduction of the Rabi splitting is observed for the lower temperatures in Fig. 5. This gives an indication that saturation occurs in our system at the few-photon level when there are a few atoms in the cavity.

We can further study the saturation behavior of the system by fitting our transmission spectra to the transfer function of an ACMRR following the Stern and Levy formalism [52] (see Supplement 1 Section 3); doing so also provides additional validation that signatures of atom-cavity interaction are observable down to the few-atom regime. We calculate the expected round-trip loss by evaluating the refractive index of Rb in the vicinity of a waveguide [22] and using it in a finite-element method simulation to extract the modal loss. The modal loss is multiplied by a free parameter to accompany the saturation effect. In Fig. 6, we present this parameter, which we term as an interaction factor, for the different measurements taken at varying cell temperatures. We then fit the data to the known expression $\alpha = \alpha_0(1/(1 + P/P_{\mathrm{sat}}))$, where α is the interaction factor, α_0 is a constant prefactor, P is the power, and P_{sat} is the saturation power. From this expression, we have extracted P_{sat} for different atomic densities. In Fig. 6(a), we display the saturation data for cell temperatures between 120°C and 70°C (corresponding to atom numbers between 180 and six), and observe a clear saturation behavior in all cases. We can still see a saturation effect at 60°C (three atoms) and 50°C (one atom) [Figs. 6(b) and 6(c)], though the uncertainty is greater. Across the full set of data, we observe saturation powers as high as 20 nW (higher temperature/atomic density) and as low as 3 nW (lowest temperatures/atomic density), which based on the conversion provided above, again indicates saturation at the few-photon level when operating with just a few atoms in the cavity.

We can estimate the expected saturation photon number n_{sat} for a single atom in the cavity using the typical expression used in cavity QED [9], given as $n_{\mathrm{sat}} = \gamma^2/(2g_0^2)$, where γ and g_0 are as previously defined, with $\gamma/2\pi = 200$ MHz due to transit time broadening. As the warm, moving atoms are interacting with different parts of the cavity field in all measurements, we estimate an average g_0 ($\bar{g}_0$) based on the Rabi splitting data taken at high temperature (100°C). We take $\bar{g}_0 = g/\sqrt{N}$, with g being half the Rabi splitting for an on-resonance transmission spectrum in Fig. 4(e). As discussed earlier, we estimate N by calculating the mode volume that can interact with the atoms (using the mode decay length) and multiplying it by the atomic density at this temperature (we choose 100°C). Using this approach, we deduce $\bar{g}_0/2\pi = 125$ MHz,

so that $n_{sat} \approx 1.3$. From the fits to the data in Figs. 6(b) and 6(c), we estimated $n_{cav} \approx 0.7$ at a vapor cell temperature of 50°C (one atom) and $n_{cav} \approx 3$ at vapor cell temperatures of 60°C to 70°C (three to six atoms in the cavity), on par with the estimated n_{sat}.

The data and fits from Fig. 6 indicate a relatively weak dependence of n_{cav} on N; this is further highlighted in Section 5 of Supplement 1 through additional analysis of the experimental data. To understand whether such behavior is to be expected, in Section 4 of Supplement 1, we present a simple model of the system based on treating the N atoms as non-interacting oscillators coupled to the cavity. Looking at the onset of saturation in this system gives rise to an expression for the saturation power (P_{sat}) in the bus waveguide, $P_{sat} \sim (1 + NC_0)^2/C_0$. For the device used in this study, at 100°C the collective cooperativity $C = NC_0 = 1.69$, so that $C_0 \approx 0.033$. This relatively small C_0 explains why P_{sat} (and n_{cav}) has a weak dependence on N, as NC_0 remains much less than one (so the numerator in P_{sat} is nearly constant) until $N \gtrsim 10$. As further discussed in Supplement 1, this model predicts a six-fold increase in the saturation power as we increase the number of atoms to ≈ 50, which is similar to the increase we observe experimentally, though we acknowledge significant deviations between the experiments and the model at highest temperatures (where n_{cav} is lower than predicted) and at lowest temperatures (where n_{cav} shows an even weaker dependence on N than predicted). Supplement 1 provides a more detailed discussion regarding the limitations of our experiments and the model, which may help explain some of the observed discrepancy.

Finally, one point of interest is in comparing the ACMRR to the ACWG with regards to single-atom operation and nonlinearity. To observe a signal at such densities with the ACWG one needs to interact with millimeter long waveguides [36], which will result in the interaction with a large ensemble of atoms. In regards to nonlinearity, saturation power at the 1 nW level has been reported for waveguide devices [22,38], and similar switching powers have been reported as well [28,34,35,53]. Thus, when it comes to realizing low power nonlinearities, the advantages of the ACMRR may be limited in comparison to the ACWG. However, for single-photon, single-atom applications such as gates and single-photon sources, the ACMRR is probably preferred.

6. DISCUSSION

In summary, we have fabricated an MRR with buried integrated heaters and bonded it to a small rubidium cell. We used fine temperature control to study the atom-light interaction and observed peak collective cooperativity $C = (5.5 \pm 0.3)$ and from this measurement inferred an average single-atom cooperativity $C_0 \approx 0.1$. We have measured our device at different atom densities and observed nonlinear interaction in the few-atom regime, with saturation observed at the few-intracavity-photon level. Such nonlinearity may already be useful for quantum applications [54,55], while collective cooperativity larger than one is already useful for ensemble-based memories [56]. The short interaction time of the atom with the cavity might limit the utility of such devices in certain applications that require long coherence times, while other applications such as photon source synchronization [57] may require fast operation. Single-atom applications such as single-photon sources still require $C_0 > 1$, which implies the need to increase the cavity quality factor to volume ratio (Q/V) by a factor of 20. In principle there are several potential routes to such performance. Chip-integrated whispering gallery mode resonators have exhibited $Q > 5 \times 10^8$ [58,59], but with 1 mm scale diameters that will cause a significant reduction in g_0; on the other hand, for the current microrings, it should be feasible to increase Q by a factor of $5 \times -10\times$ with improved fabrication to limit scattering loss [60]. Alternately, photonic crystal cavities have been used to produce a high Q/V ratio [61–63] but they generally require much more elaborate design and simulation [64] to achieve high Q compared to whispering gallery mode resonators. Photonic crystal microrings [44,45] have recently been demonstrated to preserve the high Q and straightforward design of the whispering gallery mode resonators, with devices that incorporate defect regions reducing the mode volume by more than an order of magnitude, making them a compelling candidate for further investigation and optimization.

Beyond improving cavity parameters to enable higher C_0, there are several other directions for advancing this research. Apart from the fine cavity tuning and feedback stabilization we have demonstrated, the buried integrated heaters can be used for studies of thermal desorption of Rb atoms, given the high on-chip temperatures that can be reached [49]. Alternately, adjusting the cross-section of the metal layer can reduce its resistance and allow for higher currents to be carried, enabling the generation of appreciable magnetic fields (several hundred Gauss) to produce Zeeman shifts of the Rb energy levels and enable chiral light-matter interactions [32] to be studied within this platform. Finally, improved integration of the Rb vapor cell with the integrated photonics chips, for example, using anodic bonding processes commonly used for miniaturized vapor cell clocks and sensors [31], could improve device robustness, scalability, and integration.

Funding. NIST-on-a-chip; Defense Advanced Research Projects Agency SAVaNT (ARO contract W911NF2120106).

Acknowledgment. We thank Archie Brown from Triad Technology for filling the Rb cells, and David Long and Peter Riley for helpful comments about the paper. Certain commercial products or names are identified to foster understanding. Such identification does not constitute recommendation or endorsement by NIST, nor is it intended to imply that the products or names identified are necessarily the best available for the purpose.

Disclosures. The authors declare no conflicts of interest.

Data availability. Data underlying the results presented in this paper are not publicly available at this time but may be obtained from the authors upon reasonable request.

Supplemental document. See Supplement 1 for supporting content.

REFERENCES

1. N. Gisin and R. Thew, "Quantum communication," Nat. Photonics **1**, 165–171 (2007).
2. C. Monroe, R. Raussendorf, A. Ruthven, *et al.*, "Large-scale modular quantum-computer architecture with atomic memory and photonic interconnects," Phys. Rev. A **89**, 022317 (2014).
3. R. Uppu, L. Midolo, X. Zhou, *et al.*, "Quantum-dot-based deterministic photon–emitter interfaces for scalable photonic quantum technology," Nat. Nanotechnol. **16**, 1308–1317 (2021).
4. Y. Lei, F. K. Asadi, T. Zhong, *et al.*, "Quantum optical memory for entanglement distribution," Optica **10**, 1511–1528 (2023).
5. N. Sangouard, C. Simon, H. de Riedmatten, *et al.*, "Quantum repeaters based on atomic ensembles and linear optics," Rev. Mod. Phys. **83**, 33–80 (2011).
6. I. Georgescu, S. Ashhab, and F. Nori, "Quantum simulation," Rev. Mod. Phys. **86**, 153–185 (2014).
7. A. Reiserer, "Colloquium: cavity-enhanced quantum network nodes," Rev. Mod. Phys. **94**, 041003 (2022).

8. S. Haroche and J. Raimond, *Exploring the Quantum: Atoms, Cavities, and Photons, Oxford Graduate Texts* (Oxford, 2006).
9. H. J. Kimble, "Strong interactions of single atoms and photons in cavity QED," Phys. Scripta **T76**, 127 (1998).
10. I. Aharonovich, D. Englund, and M. Toth, "Solid-state single-photon emitters," Nat. Photonics **10**, 631–641 (2016).
11. E. Janitz, M. K. Bhaskar, and L. Childress, "Cavity quantum electrodynamics with color centers in diamond," Optica **7**, 1232–1252 (2020).
12. K. Srinivasan and O. Painter, "Linear and nonlinear optical spectroscopy of a strongly coupled microdisk–quantum dot system," Nature **450**, 862–865 (2007).
13. A. Dibos, M. Raha, C. Phenicie, *et al.*, "Atomic source of single photons in the telecom band," Phys. Rev. Lett. **120**, 243601 (2018).
14. T. G. Tiecke, J. D. Thompson, N. P. de Leon, *et al.*, "Nanophotonic quantum phase switch with a single atom," Nature **508**, 241–244 (2014).
15. O. Bechler, A. Borne, S. Rosenblum, *et al.*, "A passive photon–atom qubit swap operation," Nat. Phys. **14**, 996–1000 (2018).
16. D. Chang, J. Douglas, A. González-Tudela, *et al.*, "Colloquium : quantum matter built from nanoscopic lattices of atoms and photons," Rev. Mod. Phys. **90**, 031002 (2018).
17. T. Zhong, J. M. Kindem, J. G. Bartholomew, *et al.*, "Nanophotonic rare-earth quantum memory with optically controlled retrieval," Science **357**, 1392–1395 (2017).
18. I. Craiciu, M. Lei, J. Rochman, *et al.*, "Nanophotonic quantum storage at telecommunication wavelength," Phys. Rev. Appl. **12**, 024062 (2019).
19. A. W. Elshaari, W. Pernice, K. Srinivasan, *et al.*, "Hybrid integrated quantum photonic circuits," Nat. Photonics **14**, 285–298 (2020).
20. M. Davanco, J. Liu, L. Sapienza, *et al.*, "Heterogeneous integration for on-chip quantum photonic circuits with single quantum dot devices," Nat. Commun. **8**, 889 (2017).
21. F. Najafi, J. Mower, N. C. Harris, *et al.*, "On-chip detection of non-classical light by scalable integration of single-photon detectors," Nat. Commun. **6**, 5873 (2015).
22. L. Stern, B. Desiatov, I. Goykhman, *et al.*, "Nanoscale light-matter interactions in atomic cladding waveguides," Nat. Commun. **4**, 1548 (2013).
23. R. J. Thompson, G. Rempe, and H. J. Kimble, "Observation of normal-mode splitting for an atom in an optical cavity," Phys. Rev. Lett. **68**, 1132–1135 (1992).
24. Q. A. Turchette, C. J. Hood, W. Lange, *et al.*, "Measurement of conditional phase shifts for quantum logic," Phys. Rev. Lett. **75**, 4710–4713 (1995).
25. V. Venkataraman, K. Saha, and A. L. Gaeta, "Phase modulation at the few-photon level for weak-nonlinearity-based quantum computing," Nat. Photonics **7**, 138–141 (2013).
26. C. Perrella, P. S. Light, S. A. Vahid, *et al.*, "Engineering photon-photon interactions within rubidium-filled waveguides," Phys. Rev. Appl. **9**, 044001 (2018).
27. W. Yang, D. B. Conkey, B. Wu, *et al.*, "Atomic spectroscopy on a chip," Nat. Photonics **1**, 331–335 (2007).
28. S. M. Spillane, G. S. Pati, K. Salit, *et al.*, "Observation of nonlinear optical interactions of ultralow levels of light in a tapered optical nanofiber embedded in a hot rubidium vapor," Phys. Rev. Lett. **100**, 1–4 (2008).
29. D. E. Jones, J. D. Franson, and T. B. Pittman, "Ladder-type electromagnetically induced transparency using nanofiber-guided light in a warm atomic vapor," Phys. Rev. A **92**, 043806 (2015).
30. R. Finkelstein, G. Winer, D. Z. Koplovich, *et al.*, "Super-extended nanofiber-guided field for coherent interaction with hot atoms," Optica **8**, 208–215 (2021).
31. J. Kitching, "Chip-scale atomic devices," Appl. Phys. Rev. **5**, 031302 (2018).
32. R. Zektzer, E. Talker, Y. Barash, *et al.*, "Chiral light–matter interactions in hot vapor-cladded waveguides," Optica **6**, 15–18 (2019).
33. L. Stern, M. Grajower, N. Mazurski, *et al.*, "Magnetically controlled atomic-plasmonic Fano resonances," Nano Lett. **18**, 202–207 (2018).
34. R. Zektzer, E. Talker, Y. Barash, *et al.*, "Atom–photon interactions in atomic cladded waveguides: bridging atomic and telecom technologies," ACS Photon. **8**, 879–886 (2021).
35. A. Skljarow, N. Gruhler, W. Pernice, *et al.*, "Integrating two-photon nonlinear spectroscopy of rubidium atoms with silicon photonics," Opt. Express **28**, 19593–19607 (2020).
36. L. Stern, B. Desiatov, N. Mazurski, *et al.*, "Strong coupling and high-contrast all-optical modulation in atomic cladding waveguides," Nat. Commun. **8**, 14461 (2017).
37. H. Alaeian, R. Ritter, M. Basic, *et al.*, "Cavity QED based on room temperature atoms interacting with a photonic crystal cavity: a feasibility study," Appl. Phys. B **126**, 25 (2020).
38. R. Zektzer, N. Mazurski, Y. Barash, *et al.*, "Nanoscale atomic suspended waveguides for improved vapour coherence times and optical frequency referencing," Nat. Photonics **15**, 772–779 (2021).
39. M. T. Hummon, S. Kang, D. G. Bopp, *et al.*, "Photonic chip for laser stabilization to an atomic vapor with 10^{-11} instability," Optica **5**, 443–449 (2018).
40. Y. Sebbag, E. Talker, A. Naiman, *et al.*, "Demonstration of an integrated nanophotonic chip-scale alkali vapor magnetometer using inverse design," Light Sci. Appl. **10**, 54 (2021).
41. A. Naiman, E. Talker, Y. Barash, *et al.*, "Large cooperativity in strongly coupled chip-scale photonic-atomic integrated system," Research Square (2021).
42. R. Ritter, N. Gruhler, W. H. P. Pernice, *et al.*, "Coupling thermal atomic vapor to an integrated ring resonator," New J. Phys. **18**, 103031 (2016).
43. L. Stern, R. Zektzer, N. Mazurski, *et al.*, "Enhanced light-vapor interactions and all optical switching in a chip scale micro-ring resonator coupled with atomic vapor: enhanced light-vapor interactions," Laser Photon. Rev. **10**, 1016–1022 (2016).
44. X. Lu, A. McClung, and K. Srinivasan, "High-Q slow light and its localization in a photonic crystal microring," Nat. Photonics **16**, 66–71 (2022).
45. X. Lu, F. Zhou, Y. Sun, *et al.*, "Rod and slit photonic crystal microrings for on-chip cavity quantum electrodynamics," Nanophotonics **12**, 521–529 (2023).
46. C. Alcock, V. Itkin, and M. Horrigan, "Vapour pressure equations for the metallic elements: 298–2500k," Canad. Metall. Q. **23**, 309–313 (1984).
47. R. Zektzer, L. Stern, N. Mazurski, *et al.*, "On-chip multi spectral frequency standard replication by stabilizing a microring resonator to a molecular line," Appl. Phys. Lett. **109**, 10–14 (2016).
48. K. König, P. Imgram, J. Krämer, *et al.*, "On the performance of wavelength meters: part 2—frequency-comb based characterization for more accurate absolute wavelength determinations," Appl. Phys. B **126**, 86 (2020).
49. G. Moille, D. Westly, E. F. Perez, *et al.*, "Integrated buried heaters for efficient spectral control of air-clad microresonator frequency combs," APL Photon. **7**, 126104 (2022).
50. P. Siddons, C. S. Adams, C. Ge, *et al.*, "Absolute absorption on rubidium d lines: comparison between theory and experiment," J. Phys. B **41**, 155004 (2008).
51. K. Srinivasan, C. P. Michael, R. Perahia, *et al.*, "Investigations of a coherently driven semiconductor optical cavity qed system," Phys. Rev. A **78**, 033839 (2008).
52. L. Stern and U. Levy, "Transmission and time delay properties of an integrated system consisting of atomic vapor cladding on top of a micro ring resonator," Opt. Express **20**, 28082–28093 (2012).
53. V. Venkataraman, K. Saha, P. Londero, *et al.*, "Few-photon all-optical modulation in a photonic band-gap fiber," Phys. Rev. Lett. **107**, 193902 (2011).
54. A. Pick, E. Matekole, Z. Aqua, *et al.*, "Boosting photonic quantum computation with moderate nonlinearity," Phys. Rev. Appl. **15**, 054054 (2021).
55. D. E. Chang, V. Vuletić, and M. D. Lukin, "Quantum nonlinear optics — photon by photon," Nat. Photonics **8**, 685–694 (2014).
56. M. Afzelius and C. Simon, "Impedance-matched cavity quantum memory," Phys. Rev. A **82**, 022310 (2010).
57. O. Davidson, O. Yogev, E. Poem, *et al.*, "Single-photon synchronization with a room-temperature atomic quantum memory," Phys. Rev. Lett. **131**, 033601 (2023).
58. K. Y. Yang, D. Y. Oh, S. H. Lee, *et al.*, "Bridging ultrahigh-Q devices and photonic circuits," Nat. Photonics **12**, 297–302 (2018).
59. M. W. Puckett, K. Liu, N. Chauhan, *et al.*, "422 million intrinsic quality factor planar integrated all-waveguide resonator with sub-MHz linewidth," Nat. Commun. **12**, 934 (2021).
60. X. Ji, S. Roberts, M. Corato-Zanarella, *et al.*, "Methods to achieve ultrahigh quality factor silicon nitride resonators," APL Photon. **6**, 071101 (2021).
61. K. E. Grutter, M. Davanço, and K. Srinivasan, "Si_3N_4 nanobeam optomechanical crystals," IEEE J. Sel. Top. Quantum Electron. **21**, 61–71 (2015).
62. K. Debnath, M. Clementi, T. D. Bucio, *et al.*, "Ultrahigh-Q photonic crystal cavities in silicon rich nitride," Opt. Express **25**, 27334–27340 (2017).

63. J. Zhan, Z. Jafari, S. Veilleux, *et al.*, "High-Q nanobeam cavities on a silicon nitride platform enabled by slow light," APL Photon. **5**, 066101 (2020).

64. Q. Quan and M. Loncar, "Deterministic design of wavelength scale, ultra-high Q photonic crystal nanobeam cavities," Opt. Express **19**, 18529–18542 (2011).